Title

Visualization of breast cancer metabolism using multimodal non-linear optical microscopy of cellular lipids and redox state

Journal

Cancer Research, 78(10)

ISSN

0008-5472

Authors

Hou, Jue

Williams, Joshua

Botvinick, Elliot L

et al.

Publication Date

2018-05-15

DOI

10.1158/0008-5472.can-17-2618

Peer reviewed

Visualization of breast cancer metabolism using multimodal non-linear optical microscopy of cellular lipids and redox state

Jue Hou[a], Joshua Williams[a], Elliot L. Botvinick[a,b], Eric O. Potma[a,c] and Bruce J. Tromberg[a,1]

a. Laser Microbeam and Medical Program (LAMMP), Beckman Laser Institute and Medical Clinic, University of California Irvine, Irvine, CA 92617
b. Bio-Engineering of Advanced Mechanical Systems (BEAMS) Laboratory, University of California Irvine, Irvine, CA 92617
c. Department of Chemistry, University of California Irvine, Irvine, CA 92617

Running title: Imaging cancer cellular lipids and redox state with NLOM

Key Words: Nonlinear Optical Microscopy, Cell Metabolism, Breast Cancer, 3D Culture, Cancer Invasiveness

Corresponding Author: Bruce J. Tromberg

Address: 1002 Health Sciences Rd, Irvine, CA 92617

Email: bjtrombe@uci.edu Phone: (949) 824-8705 Fax: (949) 824-8413

This work was supported by National Institute of Biomedical Imaging and Bioengineering (P41EB015890), National Cancer Institute (R01CA142989 and 1R01CA195466-01), the NCI Chao Family Comprehensive Cancer Center (P30CA62203), and Arnold and Mabel Beckman Foundation.

The authors declare no potential conflicts of interest

Word Count: 4983 4 Figures

Abstract

Label-free non-linear optical microscopy (NLOM) based on two-photon excited fluorescence (TPEF) from cofactors Nicotinamide Adenine Dinucleotide (NADH) and Flavin Adenine Dinucleotide (FAD^+) is widely used for high-resolution cellular redox imaging. In this work, we combined three, label-free NLOM imaging methods to quantitatively characterize breast cancer cells and their relative invasive potential: 1) TPEF optical redox ratio (ORR = FAD+/NADH + FAD^+), 2) coherent Raman scattering (CRS) of cellular lipids, and 3) second harmonic generation (SHG) of extracellular matrix (ECM) collagen. 3D spheroid models of primary mammary epithelial cells (PME) and breast cancer cell lines (T47D and MDA-MB-231) were characterized based on their unique ORR and lipid volume fraction signatures. Treatment with 17β-estradiol (E2) increased glycolysis in both PME and T47D ER+ breast cancer cells. However, PME cells displayed increased lipid content with no ECM effect, while T47D cells had decreased lipid storage ($p<0.001$) and significant reorganization of collagen. By measuring deuterated lipids synthesized from exogenously administered deuterium-labeled glucose, treatment of T47D cells with E2 increased both lipid synthesis and consumption rates. These results confirm that glucose is a significant source for the cellular synthesis of lipid in glycolytic breast cancer cells and that the combination of cellular redox and lipid fraction imaging endpoints is a powerful approach with new and complementary information content.

Significance

Findings provide unique insight into metabolic processes, revealing correlations between cancer metastasis and cellular redox state, lipid metabolism, and extracellular matrix.

Introduction

Despite the high rate of mutations and cell heterogeneity among tumors, nearly all cancer cells show abnormal metabolic behaviors. In 1924, Otto Warburg first reported that cancer cells prefer glycolysis as the metabolic pathway for generating chemical energy, even in an oxygen rich environment [1]. The most popular hypothesis poses that such metabolic adaptation is beneficial for fast cell proliferation, a notion supported by observations that 1) several mutations that affect cancer proliferation also regulate metabolic pathways [2, 3]; and 2) normal cells display higher rates of glycolysis when treated with growth factors to stimulate cell proliferation [4, 5]. To prepare for mitosis, doubling of the cell's biomass is required and cancer cells meet this demand by incorporating glucose as a carbon source for biosynthesis. Cancer cells are believed to actively use intermediate products of glycolysis for producing amino acids, fatty acids and nucleotides [6].

Because of the Warburg effect, glucose metabolism can be used as a biomarker for cancer diagnosis and as a probe for monitoring the response to administered cancer drugs [7, 8]. For instance, *Walsh et al.* reported decreased glycolysis rates in estrogen receptor positive (ER+) breast cancer cells compared to human epidermal growth factor receptor 2 positive (HER2+) breast cancer cells, and used glucose metabolism to differentiate breast cancer subtypes [9]. It has also been observed that invasive cancer cells exhibit increased rates of oxidative phosphorylation when peroxisome proliferator-activated receptor gamma coactivator 1-alpha (PGC-1α) expression is upregulated [10]. Despite the generality of the Warburg effect, determination of the glycolytic rate in cells alone is often insufficient to classify cell malignancy. This is because normal cells can also present a high rate of glycolysis as regulated by environment, cell function and endocrine factors [11, 12]. For example, endothelial cells display

a high glycolytic rate when phosphofructokinase-2/fructose-2,6-bisphosphatase3 (PFKFB3) activity is high, which is known to correlate with its antigenic capacity [13]. Insulin can also affect cellular glucose metabolism through sterol responsive element binding protein-1c (SREBP-1c) [14].

To improve the assessment of cellular health in the context of its glycolytic rate, glucose metabolism can be correlated with other metabolic observables in the cell. In many cancers, including breast cancer, metabolic reprogramming benefits biomolecule synthesis to meet the high demand of biomass for mitosis. In mammary epithelial cells, an important end product of cellular biosynthesis is milk fat [15]. It is well known that breast cancer is associated with altered lipid metabolism, which is manifested by changes in intracellular lipid quantities [16]. Correlating the cellular glycolytic rate to lipid metabolism in breast cells thus represents a potential strategy for assessing cell malignancy based solely on metabolic observables [17].

In this work, we used multi-modal, nonlinear optical microscopy (NLOM) to characterize both glucose and lipid metabolism in normal and breast cancer cells. Specifically, we employ two-photon excited fluorescence (TPEF) to determine the cell's optical redox ratio (ORR) as reported by the autofluorescence ratios of metabolic coenzymes (FAD^+ /(NADH+ FAD^+)) [18, 19], and coherent Raman scattering (CRS) microscopy [20, 21] to probe intracellular lipid content and *de novo* lipid synthesis. In addition, we map cell-extracellular matrix (ECM) interactions in 3D acini by visualizing second harmonic generation (SHG) signals from collagen, a major ECM component [22].

The combination of these imaging techniques enables the evaluation of glucose and lipid metabolism in live cells with minimum interruption. We examined metabolism in primary mammary epithelial (PME) cells, and in two lines of breast cancer cells derived from metastatic

sites, T47D (estrogen receptor positive) and MDA-MB-231 (triple negative) cells. To mimic the conditions in tissue, the cells were cultured in 3D in a matrigel/collagen mixture, forming physiologically-relevant acini and displaying gene expression patterns that are similar to what is seen in the body [23]. Using this platform, we showed that label-free metabolic signatures can be used to fully distinguish between mature PME, T47D and MDA-MB-231 acini. We further confirm the sensitivity of the combined glycolysis/lipid metabolism metric by observing the cellular response after treatment with 17β-estradiol (E2), showing clear changes in both cellular metabolism and ECM interactions that correlate with invasiveness. Finally, we use deuterated glucose and CRS detection to track the flow of carbon-hydrogen units in individual cells and establish a direct link between glycolytic activity, lipid synthesis and lipid consumption [24, 25].

MATERIAL AND METHODS

Nonlinear optical microscopy. A 76-MHz mode-locked Nd:Vanadate laser was used to deliver a 7-ps pulsed laser beam at 1064nm (Stokes beam) and a second harmonic generated beam at 532nm to pump an optical parametric oscillator. The OPO generated the corresponding pump beam for imaging either the normal lipid distribution (817nm) or deuterated signal (864nm) by adjusting the crystal temperature, Lyot filter and cavity length. The Stokes beam was modulated at 10MHz with an acousto-optic modulator and spatially and temporally overlapped with the pump beam before sending into a laser scanning microscope. The CARS and SRS signals were separated and detected in the forward direction. The fluorescent signals and SHG signals were collected by a commercial Zeiss laser scanning microscope (LSM510, Zeiss Inc.). The system details are described in the **Supplementary Materials and Methods**.

Materials. Deuterated glucose (552003), normal glucose (G7021), l-arginine (A5006), l-lysine (L5501) and 17β-estradiol (E8875) were purchased from Sigma-Aldrich. SILAC Advanced DMEM/F-12 flex media, no glucose, no phenol red (A2494301), TrypLE (12604013), charcoal stripped fetal bovine serum (12676011), Hanks buffer (14025092) and glutaMAX (35050-061, Life Technologies) were purchased from ThermoFisher scientific. Mammary Epithelial Cell Basal Medium (PCS-600-030) and growth kit (PCS-600-040) were purchased from ATCC. Matrigel (356231) and high concentration rat tail collagen I (354249) were purchased from Corning Inc.. The PME (PCS-600-010), T47D (HTB-133) and MDA-MB-231 cells (HTB-26) were directly purchased from ATCC. As described by ATCC, all the cell lines were authenticated by morphology, karyotyping and PCR based approaches. The cells will be cultured for 7 passages before being utilized in the experiments.

Advance DMEM/F-12 culture medium was made by adding 5% charcoal stripped FBS (vol/vol), 1% glutaMAX (vol/vol), 147.5 mg/L l-arginine, 91.25 mg/L l-lysine and 3151 mg/L normal glucose. Serum free medium was made as advanced DMEM/F-12 culture medium without FBS. Deuterated culture medium was made by replacing normal glucose with 17.5 mM deuterated glucose. 17β-estradiol was dissolved in DMSO at 10^{-8} M. The cells were sent to ATCC for Hochest DNA stain to clear for mycoplasma before growing in the lab. We did not use antibiotics during regular cell culture and the contamination was identified on conventional microscope. The cells will be discarded when any contamination were noticed.

3D breast cancer model. Matrigel was thawed on ice for 12 hours before the experiment. The pipet tips and imaging dishes (7160-2, Miltenyi Biotes) were chilled in -20 ˚C overnight. The high concentration rat tail collagen I was diluted to 3.2mg/ml by following the manual provided

on the website. Both the matrigel and collagen were mixed with 1:1 ratio to match up with the mechanical properties of extracellular matrix. Imaging dishes were coated with 50ul matrigel/collagen mixture and left in the incubator for 1 hour to become solidify. Cells were detached from plates using TripLE, stain with trypan blue and counted with a hemacytometer. The experiment would continue only if the cell live rate was above 90%. The cells were collected and gently pelleted by centrifugation at 1000rpm for 8 minutes. The medium was aspirated and the cells were suspended in 500ul matrigel/collagen mixture and plated onto the coated imaging dishes. The plating cell concentrations were 100k/well for PME cells and 60k/well for T47D and MDA-MB-231 cells. The dishes were put in the incubator for an hour to gel before adding 2ml culture medium. The cells were incubated at 37 ˚C, 5% CO2 and the medium is changed every three days. For each cell lines, three identical imaging dished were prepared. To introduce cancer invasiveness in T47D cell lines, 10^{-8} M 17β-estradiol was added to the culture medium.

Metabolic measurements of the acini. To track metabolic changes during the acini formation, fifteen different PME acini structures were randomly chosen from each imaging dish. The entire 3D volume of acinus structure was imaged with 1um z-step for both glucose and lipid metabolism. To compare the metabolic signatures of PME, T47D and MDA-MB-231 cells, 15 acini from each group were imaged after 12 days of culturing. The redox ratio and lipid content of each acinus was calculated as described in detail below. To study the metabolic changes in response to E2, we added 17β-estradiol (10^{-8} M) to both PME and T47D 3D cultures. The metabolism of 15 randomly chosen acini were measured before adding E2 and 3 days after adding E2. The experiments conducted were summarized in Table S1.

Lipid synthesis from deuterated glucose. The cells were seeded in 24-well plates at 50,000 cells/well with 1mL advanced DMEM culture medium. For lipid dynamic studies, the culture medium was changed to serum free medium for cell cycle synchronization for 12 hours [26]. After synchronization, the control groups (6 wells) were replaced with deuterated culture medium and DMSO and the experimental groups (6 wells) were replaced with deuterated culture medium and 17β-estradiol (10^{-8} M). After 24 hours of culturing, we switched all the wells to normal advanced DMEM/F-12 culture medium (considered T=0). We fixed one well in each group at times T=0h, 3h, 6h, 9h, 12h and 24h. For the experiment that studied the correlation between glucose metabolism and lipid synthesis rate, cells were prepared in the same way in 6 imaging dishes (3 control dishes and 3 experiment dishes). The cells were kept constant at 37°C and imaged with TPEF following SRS imaging. Five locations were randomly imaged in each well or imaging dish.

Acini quantification. The 3D culture dishes were mounted on a conventional bright field microscope and five locations were randomly imaged using a 25x objective. In each location, we manually adjusted the objective axial position and counted the number of acini spheroids and broken acini at different depths in the ECM. The fraction of broken acini was calculated as the ratio of broken acini over total acini structures.

Image processing. For TPEF images, the background noise, cytoplasm, and cell nucleus were separated by the three component Otsu algorithm. The ORR optical redox ratio ($FAD^+/(NADH+FAD^+)$) was calculated in the cytoplasm regions pixel by pixel. For CARS

images, a four-component (background, cell nuclei, cytoplasm and lipid droplets) Otsu thresholding algorithm was used to determine the area of cytoplasm and lipids. We use the number of pixels of lipid droplets over the number of pixels of cytoplasm to estimate the lipid percentage. For cells cultured in 3D, lipid content at each depth was evaluated separately and the total lipid percentage was calculated as the summation of pixels of lipid droplets over the 3D volume of the acini. For SRS images, we manually selected the lipid droplets and used the average intensities within the regions of interest to calculate the dLD/LD ratios. Fifteen to twenty different droplets were analyzed in each field of view and fifty droplets were included for statistical analysis for each group. The collagen fiber orientation was quantified with a customized Matlab program based on an algorithm previously published [27]. The program was explained in detail in **Supplementary Materials and Methods.**

Statistical analyses. The redox ratio and lipid percentage measurements during acini formation were tested with a linear mixed model to validate the increasing trend of metabolic rate at different days. The metabolic measurements between different cell lines and before and after drug treatments were tested with two component ANVOA tests. A significance level less than 0.05 was used for all statistical analyses.

Results

Metabolic changes during acinus formation

We used NLOM imaging to monitor the metabolic changes of PME cells during the formation of acini (fig. 1). Two-photon excited fluoresce (TPEF) was used to measure the optical redox ratio ($ORR = FAD^{+}/(NADH + FAD^{+})$) while lipid content was measured using coherent anti-Stokes

Raman scattering (CARS). Fifteen randomly chosen acini were followed every other day for 12 days. Figure 1a-f shows ORR distributions and CARS images of cross sections of one representative PME acinus at days 4, 8 and 12.

PME cells had low optical redox ratios when first seeded into the matrigel/collagen mixture. Average ORRs started to increase but were not significantly different over the first three days. On day 4, we observed early formation of spheroids by multiple PME cells with homogeneous ORR values. From day 4 to day 10, the spheroids grew larger and the average ORR rose from 0.15 to 0.19 ($p<0.01$). Cell clusters started to display spatial variations in the metabolic distribution around day 8 (fig 1d) with ORR increasing from exterior to interior. The two distinct cell populations contributed to the observed increase in standard deviation of the mean ORR on day 8. Cell metabolism remained on the same level from day 10 to day 12. Moreover, the cells in the center that demonstrated abnormally high optical redox ratios disappeared and left a hollowed center (fig 1g). A single layer of PME cells formed alveolar structures that strongly mimicked normal mammary glands. Interestingly, a polarized metabolic signature was not observed during spheroid-formation for the T47D cancer cell line during the entire experiment indicating that this polarized phenotype is specific to normal mammary epithelial cells (fig S1 a and b). In PME cells, ORR values in the remaining cells increased by ~50% compared to initial seeding cells. Both T47D and MDA-MB-231 cancer cells also had increasing ORR levels during the 12 days of culturing with different slopes and plateau values (fig S1 c and d).

We also observed an increase in cytoplasmic lipid content during acinus formation. Typical CARS cross-sectional images are shown in fig 1b, d and f. The bright spots are CARS signals from lipid droplets while the overall cell morphology can be visualized by the non-

resonant CARS background. We observed near-zero lipid content in cells first seeded into the gel. However, the cells started to accumulate lipid at day 4 and the total amount of lipid droplets increased ~10 fold after another 6 days of culturing. The total lipid content reached a plateau and became stabilized after 12 days of culturing.

NLOM provided sufficiently high spatial and temporal resolution to observe coordinated changes in glucose and lipid metabolism in single cells during the process of acinus formation. A linear mixed model was used to show that both the ORR and lipid content increased significantly over time ($p<0.01$). Multiple stages of development were observed, suggesting that a minimum time is required for each acinus to become mature. For this purpose, all of the subsequent experiments were conducted on acini cultured for 12 days.

Metabolic signatures between different cell lines

We also measured the metabolic signatures in 3D spheroids for different breast cell lines. Figure 2 shows TPEF images (a-c) and CARS images (d-f) corresponding to the cross sections of PME, T47D and MDA-MB-231 cells cultured in 3D on day 12. Different cell lines displayed varying morphologic features determined by their pathologic characteristics. As described above, normal cells form spheroids with a hollow center that mimic normal mammary alveolar structures (fig. 2a and d). However, the highly proliferative T47D ER+ breast cancer cells formed spheroid structures but with a solid center filled with cells (fig. 2b and e). The highly metastatic triple negative MDA-MB-231 cancer cells did not form any growth-arrested structures and spread out through the entire matrix (fig 2c and f).

Aside from these morphological differences, the three different cell lines had different metabolic signatures corresponding to their phenotypes. In figure 2g, the average ORR and lipid

content of each cell line are compared. The ORR for normal breast epithelial cells (PME) was significantly higher than for the two malignant cancer cell lines ($p<0.01$). The ER+ T47D cell lines were the most glycolytic (lowest ORR), while the ORR for MDA-MB-231 was significantly higher than for T47D cells ($p=0.013$) but lower than normal. Our observations not only show that the cancer cells are more glycolytic compared with normal cells (Warburg effect) but also demonstrate that glucose metabolism can vary between breast cancer subtypes. Lipid content from the same acini was measured using CARS. All the breast cancer cell lines exhibited much lower lipid storage compared with normal breast cells. The lipid content in the PME cells was 2.5 times higher than in the T47D cell lines; and the triple negative breast cancer cells had a lipid storage fraction close to 0 (fig. 2d-f). The three cell lines demonstrated dramatic differences in lipid droplet content and were well-separated with this parameter (fig. 2g).

After combining the glucose and lipid metabolism of each acinus, we constructed a metabolic "map" with axes representing ORR and lipid content (fig 2h). Each dot in the scatterplot is derived from measurements of one acinus on day 12 (~50-200 cells per acinus). As shown in the figure, PME, T47D and MDA-MB-231 cells were clearly distinguishable in the 2D scatterplot based on their metabolic signatures.

Impact of Estradiol on metabolic signatures

17β-estradiol (E2) is known to increase invasiveness in ER+ breast cancers and affects response to chemotherapy [28]. However, the presence of E2 is crucial for normal organ development and function including breast milk secretion [29, 30]. We added 17β-estradiol to both mature T47D (ER+ breast cancer cell lines) and PME (normal) acini at physiologically relevant concentrations (10^{-8} M) and monitored the acini morphological and metabolic responses for 3 days.

The PME cells did not show any morphology change with or without E2 (fig. 3a and b). However, the T47D breast cancer cells demonstrated a higher fraction of broken acini ($p<0.01$) and a remodeling of the collagen fibers, signatures of increased invasiveness. In the control group (untreated with E2), 78% of the T47D cell clusters remained as spheroids which were wrapped with arbitrarily oriented collagen fibers (fig. 3c). The 3D reconstruction of T47D treated with DMSO and E2 are demonstrated (supplementary video 1 and 2). However, 84% of the acini were no longer growth arrested and showed one or more extrusions of cancer cells after E2 treatment (fig. 3d). All the treated spheroids exhibited a visible remodeling of the ECM at the broken sites. Before E2 treatment, collagen fibers organized in a direction normal to the spheroid surface (fig. 3e). In the growth-arrested region of the broken acini (fig. 3f), we observed increased collagen fiber alignment compared to pre-treatment, however this was not as dramatic as the extruded cells. After treatment, fibers were highly polarized and aligned in the direction of extruded cancer cells in the broken acini (fig. 3g), a structural feature that can benefit invasion [31].

Glucose and lipid metabolism were recorded for both PME and T47D cells treated with either DMSO (control) or E2 (fig 3h). The optical redox ratio of E2-treated PME cells decreased slightly from 0.34 to 0.32 ($p=0.04$), however the ORR of T47D cancer cells dropped about 30% ($p<0.01$) when treated with E2. In contrast, lipid droplet content *increased* significantly in E2-treated PME cells ($p=0.02$) while the lipid content of T47D cells *diminished* by half ($p=0.03$). The effects of E2 on cell metabolism are shown in a metabolic scatter map and trends denoted with arrows (fig 3i). An increase in cancer invasiveness is observed to accompany metabolic adaptations to E2, wherein cancer cells become more glycolytic and have lower lipid content.

Despite E2 stimulation, PME cells preserve acini structural integrity and demonstrate significant lipid accumulation that matches normal mammary epithelial cell function.

Evaluating lipid synthesis and utilization rates

Our NLOM redox measurements are consistent with cancer cell Warburg metabolism as observed in previous studies [4]. However, it is unclear from our lipid imaging results whether the inverse relationship between lipid accumulation and invasiveness is a consequence of impaired storage/synthesis or enhanced lipid utilization. In order to further explore these signatures, we used deuterium labeling and stimulated Raman scattering (SRS) microscopy to track carbon flow starting from glucose [24]. Deuterium labeling shifts the resonances of chemical group vibrations to regions of the vibrational spectrum devoid of overlapping Raman modes, enabling a virtually background-free detection of the targeted chemical groups. SRS microscopy probes different chemical vibrations by adjusting the optical frequency difference between two incident laser beams (pump and Stokes). In our experiment, we kept the optical frequency of the Stokes beam constant and tuned the optical frequency of the pump beam to image both natural aliphatic lipids (Raman shift is 2850 cm-1) and deuterated hydro-carbons (Raman shift is 2175 cm-1). By doing so, we are able to specifically monitor the newly synthesized fatty acids from deuterated glucose since the signal intensity is directly related to the amount of deuterium labeled carbons incorporated from glucose.

We first tested the system sensitivity by imaging the T47D cancer cells cultured in normal and deuterated glucose medium. The SRS images of cells cultured under both conditions exhibited similar levels of normal lipid droplet formation (fig. S2a and b) but only the cells cultured with deuterated glucose exhibited signals at the Raman shift of 2175 cm^{-1} (fig. S2c and

d). The Raman spectrum of droplets with deuterated material (pointed out by the arrow) was distinct from the Raman spectrum of deuterated glucose (fig. S2e), underscoring that the hydrocarbon units originally derived from glucose were incorporated in newly synthesized and chemically distinct compounds in the droplets. We also collected hyperspectral SRS images in the 2800 cm^{-1} to 3050 cm^{-1} range and identified three major chemicals (lipid, water and protein) by vertex component analysis. The deuterated compounds were found to co-localize only with lipid droplets (red) and confirmed the system's capability to track the flow of carbon in live cells for lipid synthesis (fig. S2f-i).

PME, T47D and T47D breast cancer cells treated with E2 were cultured in 2D with deuterated glucose medium. After incubation for 12 hours, we measured the ORR, normal lipid droplet fraction (LD), and deuterated lipid droplet fraction (dLD) in the three groups (fig. 4). The amount of glucose-derived lipid was evaluated with the ratios of dLD/LD. Figure 4 a-c shows representative SRS images of normal lipid distribution for each group. The glucose-derived lipid droplets were visualized in the deuterium region (fig. 4d-f). Moreover, we observed newly synthesized lipid deposited at the outside of existing lipid droplets which formed donut-shaped dLDs (fig. 4f inset). PME cells exhibited ~3-fold greater levels of normal lipid accumulation compared with T47D cells ($p<0.01$). The normal lipid content further decreased by 58% in the T47D cells treated with E2. However, T47D cells had elevated levels of deuterated lipids and the dLD/LD ratios were 5 times higher compared with PME cells (fig.4 d and e). ER activated cancer cells exhibited stronger deuterated lipid signal intensities and the average dLD/LD ratio was 1.4 times higher ($p=0.03$), indicating increased lipid synthesis rates.

To probe the lipid utilization rate with and without ER activation, we performed a pulse-chase experiment. T47D cells were first exposed to deuterated glucose medium for ~12 hours

before switching to normal glucose medium. The SRS images of normal cellular lipid content and deuterated lipids were acquired at different time points to determine the average intensity ratios of dLD/LD. Figure 4g-i shows representative images of deuterated signals measured at T = 0h, 6h and 12h. The deuterated signals exhibited exponential decays among which the E2 treatment increased lipid turnover rate by 3 hours (fig. 4j). The lipid decay rate in cancer cells treated with E2 ($k=0.26 \pm 0.02$) was 68% faster than in cells treated with DMSO ($k=0.18 \pm 0.01$), corresponding to a lipid turnover rate that is shorter by ~3 hours. The dLD/LD ratios of the two groups were log-transformed and the decay rates tested with one-way analysis of covariance revealing significant differences ($p=0.04$).

ORR measurements were consistent with results obtained from our measurements of 3D acini. PME cells have ~20% higher optical redox ratios (greater oxidative phosphorylation) compared to the more glycolytic T47D cancer cells and the ORR further decreased by 28% ($p<0.01$) in T47D cells treated with E2 (fig. 4k). Furthermore, the higher the ORR, the lower the dLD/LD (fig. 4l). Thus, the increased glycolytic rate is positively correlated with *de novo* lipid synthesis. When exogenously stimulated with E2, cancer cells adapted with increased aerobic glycolysis to benefit biosynthesis. Normal cells, in contrast, mainly relied on fatty acid uptake from the environment rather than the *de novo* lipid synthesis observed in cancer cells.

Discussion and Conclusion

Technologies such as positron emission tomography (PET), magnetic resonance spectroscopy (MRS) and mass spectrometry (MS), are also used to characterize tumor metabolism. While MS is principally employed in basic research, PET measurements of 18-Fluorodeoxyglucose (18FDG) uptake are the cornerstone of clinical metabolic imaging and new

MRS approaches utilizing hyperpolarized 13C-labeled substrates (e.g. pyruvate) with dynamic nuclear polarization (DNP) detection are emerging [32]. Multi-modal NLOM complements these technologies by measuring glycolytic state and tracking carbon-hydrogen flow with subcellular resolution in dynamic living systems, which cannot be achieved using other methods. Together, these metabolic imaging approaches provide a more complete picture of cellular and tumor metabolism across spatial and temporal scales. Their integrated use can reveal clinically-relevant features that can potentially be used to develop new prognostic markers and optimize therapeutic strategies for individual patients.

In order to establish the sensitivity of multi-modal NLOM to multiple metabolic changes at the single cell level, we visualized normal acinus formation, tumor spheroid growth, and cancer cell proliferation. Using CRS and TPEF microscopy, we captured glucose and lipid metabolic differences between normal primary mammary epithelial cells and two different cancer cell lines. In addition, we observed the differential impact of hormonal stimulation on normal vs cancer cells grown in a 3D collagen-rich matrix. Making use of deuterium labeling of glucose, we observed a correlation between cancer cell metabolism and cancer invasiveness, which originated from the utilization of glucose-derived carbons in support of cellular biosynthesis.

Normal mammary epithelial cells exhibit three distinct metabolic phases during acinus formation, characterized by gradually increasing lipid accumulation and progressive redox state changes from glycolysis to oxidative phosphorylation (Fig. 1). Early in the process (days 1-4), cells have lower optical redox ratios and low lipid accumulation. At this stage, acini are composed of 1-8 cells each with significant cell-ECM contact but little cell-cell interaction. Interactions with the ECM and the low activation of focal adhesion kinase (FAK) promotes cell

cycle progression [33]. Under these conditions, cells start to prepare for proliferation by increasing biosynthesis of DNA, organelles, membranes, *etc*. To meet the high demand for biomass, glucose is utilized not only for providing energy but also as a source of carbon-based biomass. The metabolite of glucose, citrate, is converted to acetyl-CoA and used for lipid and nucleotide production [34]. The amount of lipid droplets stored in the cytoplasm is seen to decrease, either to fuel biological activities or to synthesize cell membranes. As the acini grow, cell-cell contact arrests/inhibits proliferation rates through the Hippo/YAP pathway [35]. At this time point, the cells no longer need large amounts of biomolecule synthesis and switch back to oxidative phosphorylation to more efficiently produce ATP. Due to the low usage of lipid, the lipid droplets reappear in the cytosol. This stage of the acinus growth process gives rise to an increase in the optical redox ratio and lipid content from day 4 to day 8, when the acini generally grow to a size of 18-24 cells. Finally, by day 10-12, both the ORR and lipid content are stabilized, indicating the formation of a mature acinus.

Interestingly, we observe spatial variations in metabolism in the polarized acinus around day 8. The ORR images reveal that apical cells in the center have a higher oxidative rate while the peripheral basal cells are more glycolytic. This is likely due to gradients that drive nutrient and signaling differences. Tissue polarity has been shown to be essential for mammary epithelial cells to form healthy alveolar structures and maintain normal breast function [36]. Only basal cells are directly exposed to signaling from the ECM, especially from the binding of β4 integrin and laminin I [37]. The cells in the center of the acinus have high cell contact inhibition and lack hemidesmosome formation and NFκB activation which promotes cell apoptosis [38]. These cells exhibit increased ORR levels and disappear in 2-4 days, leaving a hollow center in the acinus. Indeed, the increase of ORR is a predictor for cell apoptosis [39].

Compared to normal epithelial breast cells, acini formed from cancer cells display altered morphologies. The T47D acinus has a solid core whereas acini grown from MDA-MB-231 cells feature irregular shapes. The appearance of cells in our 3D cultures strongly mimics observations from patient biopsies; normal breast tissue features tubular alveolar structures, ductal carcinoma *in situ* presents cell proliferation towards the lumen, and the cancer cells in invasive ductal carcinoma infiltrate into the stromal tissue [40]. We observe that each cell line examined here has distinctive NLOM-derived metabolic signatures. As predicted by the Warburg effect, T47D and MDA-MB-231 cancer cells are found to be more glycolytic compared to normal breast cells. The two malignant cancer cell lines are also characterized by significantly different optical redox ratios. Previous studies reported similar observations by monitoring glucose metabolism alone to separate distinct breast cancer subtypes [9, 41]. Our study expands on previous work by adding lipid content as an additional defining feature, motivated by recent work that suggests that abnormal lipid metabolism can be another hallmark for various cancers [42]. Cancer cells prefer *de novo* lipid synthesis and have been observed to upregulate fatty acid synthesis (FASN) enzyme expression. ERBB2, PI3K, ATP citrate lyase and various reported mutations in cancers are also known to affect lipid metabolism [16]. Thus, the combination of lipid content and ORR provides additional quantitative information that refines our ability to characterize cancer cell metabolism beyond what can be determined from each parameter separately.

Metabolic and ECM changes in response to 17β-estradiol (E2) stimulation further reveal key differences between normal and breast cancer cells. The disruption of T47D spheroid structures and remodeled collagen polarization upon treatment of E2 have been linked to increased cancer invasiveness both *in vitro* and *in vivo* [43, 44]. We observe that T47D cancer cells grow more glycolytic and display a decreased level of lipid content after E2 treatment. Our

observation is consistent with Ostrander *et al*. who reported that the expression and blocking of the estrogen receptor in ER+ cancer cells decreases the ORR, a metric that may serve as a biomarker for cancer invasiveness [45]. However, the ORR alone is insufficient for separating breast cancer from normal epithelial cells since both cell lines become more glycolytic in response to E2 treatment. Only by considering lipid storage of the two cell lines as an additional differentiator could the two populations be seen moving in different directions on the 2D-metabolic map (figure 3d). Our observations support the notion that with increased glycolysis, more glucose is used for *de novo* fatty acid synthesis in both cancer and normal cell lines [46]. Nonetheless, whereas the PME cells preserve the lipid and prepare for milk secretion, cancer cells utilize lipids to prepare for cell proliferation (i.e. producing cell membrane). This is consistent with previous magnetic resonance spectroscopy studies showing that a decrease in neutral lipid accumulation in the cytoplasm is correlated with increased cell proliferation and malignancy [47, 48].

The correlation between lipid metabolism and cancer invasiveness was further explored in CRS imaging studies in which deuterated glucose is used to track carbon flow. The utilization of deuterium labeling in combination with Raman based imaging has been demonstrated for singling out compounds of interest against the background by multiple groups [24, 25]. In this study, we push the principle of deuterium labeling one step further by combining with TPEF based ORR measurements to quantitatively characterize the correlation between glucose metabolism and lipid biosynthesis. Low deuterium signals in PME cell lipid droplets and higher dLD/LD values in T47D cells imply that cancer cells actively utilize deuterium-labeled carbons from glucose for *de novo* lipid synthesis. These results are in agreement with previous studies

showing that normal cells preferentially take up circulating fatty acids while >90% of lipid in cancer cells is synthesized from glucose and intermediate products of glycolysis [49].

While untreated T47D breast cancer cells show moderate levels of dLD/LD and an intermediate optical redox ratio, E2-treated T47D cells display the highest dLD/LD, lowest ORR, and lowest unlabeled lipid droplet accumulation. Furthermore, in our pulse-chase study, the rate of disappearance of deuterated lipid following unlabeled glucose exposure is significantly higher for E2-treated cells ($k=0.26 \pm 0.02$) *vs* cells treated with DMSO ($k=0.18 \pm 0.01$). We conclude that cancer cells treated with E2 have increased lipid synthesis rates (elevated dLD/LD), faster lipid utilization rates ($k = 0.26 \pm 0.02$), and higher glycolytic activity (lower ORR) compared to PME and untreated T47D cells.

Potential limitations to this work include the use of 2D culture for deuterated glucose studies while 3D culture was used for other experiments. This was done to improve the deuterated signal-to-background contrast and enable the detection of lipid synthesis/utilization rates with higher accuracy and sensitivity. As a result, our hypothesized direct relationship between lipid utilization rates and cancer cell invasiveness should be confirmed in future studies with 3D cell cultures. Although the presence of deuterated lipid in T47D cells clearly shows that they utilize glucose for lipid synthesis while normal PME cells do not, further studies of both normal and cancer cells and the role of other substrates, such as glutamine, that are known to impact cancer metabolism are needed to broaden this observation. As expected, E2 administration enhanced the abnormal glucose-to-lipid synthesis pathway in ER+ cancer cells, confirming the sensitivity of CRS and deuterated glucose to track carbon flow. However, we have not addressed whether E2 stimulates de novo lipid formation in PME cells or whether this process results entirely from environment-derived lipids. Finally, we routinely interpret low and

high ORR values in the context of glycolytic vs. oxidative metabolism, respectively. In order to establish this correlation, we previously validated ORR vs. conventional Seahorse flux analyzer measurements [21]. Similar observations have been made in other independent studies [50]. However, because other metabolic pathways can affect ORR and each system is unique, there is a possibility that reduced ORR values may not always represent increased glycolysis.

In conclusion, we have described a series of quantitative optical imaging endpoints that provide direct evidence of the metabolic consequences of aerobic glycolysis and the Warburg effect. Our results suggest that both lipid synthesis and utilization rates in cancer cells increase to meet greater demands for biomass and energy. To meet these demands, cancer cells become more glycolytic to generate carbon sources for biosynthesis, while the rate of utilization of stored lipid is accelerated in order to produce materials for either beta-oxidation or building blocks for cell organelles. These observations highlight the importance of multi-modal, label-free NLOM for characterizing complex metabolic pathways in cancer cells and 3D engineered cancer models.

Reference

1. Warburg, O., K. Posener, and E. Negelein, *On the metabolism of carcinoma cells.* Biochemische Zeitschrift, 1924. **152**: p. 309-344.
2. Manning, B.D. and L.C. Cantley, *AKT/PKB signaling: navigating downstream.* Cell, 2007. **129**(7): p. 1261-74.
3. Matoba, S., et al., *p53 regulates mitochondrial respiration.* Science, 2006. **312**(5780): p. 1650-3.
4. Lunt, S.Y. and M.G. Vander Heiden, *Aerobic glycolysis: meeting the metabolic requirements of cell proliferation.* Annu Rev Cell Dev Biol, 2011. **27**: p. 441-64.
5. Clemens, M.J., *Targets and mechanisms for the regulation of translation in malignant transformation.* Oncogene, 2004. **23**(18): p. 3180-8.
6. Vander Heiden, M.G., L.C. Cantley, and C.B. Thompson, *Understanding the Warburg effect: the metabolic requirements of cell proliferation.* Science, 2009. **324**(5930): p. 1029-33.
7. Munoz-Pinedo, C., N. El Mjiyad, and J.E. Ricci, *Cancer metabolism: current perspectives and future directions.* Cell Death Dis, 2012. **3**: p. e248.
8. Sebastian, C., *Tracking down the origin of cancer: metabolic reprogramming as a driver of stemness and tumorigenesis.* Crit Rev Oncog, 2014. **19**(5): p. 363-82.
9. Walsh, A.J., et al., *Optical metabolic imaging identifies glycolytic levels, subtypes, and early-treatment response in breast cancer.* Cancer Res, 2013. **73**(20): p. 6164-74.
10. LeBleu, V.S., et al., *PGC-1alpha mediates mitochondrial biogenesis and oxidative phosphorylation in cancer cells to promote metastasis.* Nat Cell Biol, 2014. **16**(10): p. 992-1003, 1-15.
11. Parra-Bonilla, G., et al., *Critical role for lactate dehydrogenase A in aerobic glycolysis that sustains pulmonary microvascular endothelial cell proliferation.* Am J Physiol Lung Cell Mol Physiol, 2010. **299**(4): p. L513-22.
12. Vazquez-Martin, A., et al., *The mitochondrial H(+)-ATP synthase and the lipogenic switch: new core components of metabolic reprogramming in induced pluripotent stem (iPS) cells.* Cell Cycle, 2013. **12**(2): p. 207-18.
13. De Bock, K., et al., *Role of PFKFB3-driven glycolysis in vessel sprouting.* Cell, 2013. **154**(3): p. 651-63.
14. Ferre, P. and F. Foufelle, *SREBP-1c transcription factor and lipid homeostasis: clinical perspective.* Horm Res, 2007. **68**(2): p. 72-82.
15. Anderson, S.M., et al., *Key stages in mammary gland development. Secretory activation in the mammary gland: it's not just about milk protein synthesis!* Breast Cancer Res, 2007. **9**(1): p. 204.
16. Menendez, J.A. and R. Lupu, *Fatty acid synthase and the lipogenic phenotype in cancer pathogenesis.* Nat Rev Cancer, 2007. **7**(10): p. 763-77.
17. Li, Z. and Y.B. Kang, *Lipid Metabolism Fuels Cancer's Spread.* Cell Metabolism, 2017. **25**(2): p. 228-230.
18. Georgakoudi, I. and K.P. Quinn, *Optical imaging using endogenous contrast to assess metabolic state.* Annu Rev Biomed Eng, 2012. **14**: p. 351-67.
19. Hou, J., et al., *Correlating two-photon excited fluorescence imaging of breast cancer cellular redox state with seahorse flux analysis of normalized cellular oxygen consumption.* J Biomed Opt, 2016. **21**(6): p. 60503.

20. Jeffrey L. Suhalim, C.-Y.C., Magnus B. Lilledahl, Ryan S. Lim, Moshe Levi,k Bruce J. Tromberg, and Eric O. Potma, *Characterization of Cholesterol Crystals in Atherosclerotic Plaques Using Stimulated Raman Scattering and Second-Harmonic Generation Microscopy.* Biophysical Journal, 2012. **102**: p. 1988-1995.
21. Alfonso-Garcia, A., et al., *Biological imaging with coherent Raman scattering microscopy: a tutorial.* J Biomed Opt, 2014. **19**(7): p. 71407.
22. Paolo P. Provenzano, K.W.E., Long Yan, Aude Ada-Nguema, Matthew W. Conklin, David R. Inman, and Patricia J. Keely, *Nonlinear Optical Imaging of Cellular Processes in Breast Cancer.* Microscopy Microanalysis, 2008. **14**: p. 16.
23. Bissell, C.M.G.M.J., *Extracellular matrix control of mammary gland morphogenesis and tumorigenesis: insights from imaging.* Histochem Cell Biol, 2008. **130**: p. 13.
24. Li, J. and J.X. Cheng, *Direct visualization of de novo lipogenesis in single living cells.* Sci Rep, 2014. **4**: p. 6807.
25. Wei, L., et al., *Imaging complex protein metabolism in live organisms by stimulated Raman scattering microscopy with isotope labeling.* ACS Chem Biol, 2015. **10**(3): p. 901-8.
26. Rosner, M., K. Schipany, and M. Hengstschlager, *Merging high-quality biochemical fractionation with a refined flow cytometry approach to monitor nucleocytoplasmic protein expression throughout the unperturbed mammalian cell cycle.* Nat Protoc, 2013. **8**(3): p. 602-26.
27. Quinn, K.P. and I. Georgakoudi, *Rapid quantification of pixel-wise fiber orientation data in micrographs.* J Biomed Opt, 2013. **18**(4): p. 046003.
28. Razandi, M., et al., *Tamoxifen regulates cell fate through mitochondrial estrogen receptor beta in breast cancer.* Oncogene, 2013. **32**(27): p. 3274-85.
29. Pedram, A., et al., *Membrane-localized estrogen receptor alpha is required for normal organ development and function.* Dev Cell, 2014. **29**(4): p. 482-90.
30. Mady, E.A., E.E. Ramadan, and A.A. Ossman, *Sex steroid hormones in serum and tissue of benign and malignant breast tumor patients.* Dis Markers, 2000. **16**(3-4): p. 151-7.
31. Aguilera, K.Y., et al., *Collagen Signaling Enhances Tumor Progression after Anti-VEGF Therapy in a Murine Model of Pancreatic Ductal Adenocarcinoma.* Cancer Research, 2014. **74**(4): p. 1032-1044.
32. Serrao, E.M. and K.M. Brindle, *Potential Clinical Roles for Metabolic Imaging with Hyperpolarized [1-(13)C]Pyruvate.* Front Oncol, 2016. **6**: p. 59.
33. Reiske, H.R., et al., *Analysis of FAK-associated signaling pathways in the regulation of cell cycle progression.* Febs Letters, 2000. **486**(3): p. 275-280.
34. Lloyd, S.M., J. Arnold, and A. Sreekumar, *Metabolomic profiling of hormone-dependent cancers: a bird's eye view.* Trends Endocrinol Metab, 2015. **26**(9): p. 477-85.
35. Gerard, C. and A. Goldbeter, *The balance between cell cycle arrest and cell proliferation: control by the extracellular matrix and by contact inhibition.* Interface Focus, 2014. **4**(3).
36. Sobolewska, A., T. Motyl, and M. Gajewska, *Role and regulation of autophagy in the development of acinar structures formed by bovine BME-UV1 mammary epithelial cells.* Eur J Cell Biol, 2011. **90**(10): p. 854-64.
37. Valerie M. Weaver, S.L., Johnathon N. Lakins, Micah A. Chrenek, Jonathan C.R. Jones, Filippo Giancotti, Zena Werb, and Mina J. Bissell, *β4 integrin-dependent formation of polarized three-dimensional architecture confers resistance to apoptosis in normal and malignant mammary epithelium.* cancer cell, 2002. **2**(3): p. 11.
38. Clarkson, R.W.E., et al., *NF-kappa B inhibits apoptosis in murine mammary epithelia.* Journal of Biological Chemistry, 2000. **275**(17): p. 12737-12742.
39. Ghukasyan, V.V. and A.A. Heikal, *Natural biomarkers for cellular metabolism : biology, techniques, and applications*. 2015.

40. Weigelt, B., F.C. Geyer, and J.S. Reis-Filho, *Histological types of breast cancer: how special are they?* Mol Oncol, 2010. **4**(3): p. 192-208.
41. Melissa C. Skala, K.M.R., Annette Gendron-Fitzpatrick, Jens Eickhoff, Kevin W. Eliceiri, John G. White, and Nirmala Ramanujam, *In vivo multiphoton microscopy of NADH and FAD redox states, fluorescence lifetimes, and cellular morphology in precancerous epithelia.* PNAS, 2007. **104**(49): p. 19494-19499.
42. Claudia Nieva, M.M., Naiara Santana-Codina, Satish Rao, Dmitri Petrov, Angels Sierra, *The Lipid Phenotype of Breast Cancer Cells Characterized by Raman Microspectroscopy: Towards a Stratification of Malignancy.* PLOS ONE, 2012. **7**(10): p. 10.
43. Kenny, P.A., et al., *The morphologies of breast cancer cell lines in three-dimensional assays correlate with their profiles of gene expression.* Mol Oncol, 2007. **1**(1): p. 84-96.
44. Brabrand, A., et al., *Alterations in collagen fibre patterns in breast cancer. A premise for tumour invasiveness?* Apmis, 2015. **123**(1): p. 1-8.
45. Ostrander, J.H., et al., *Optical redox ratio differentiates breast cancer cell lines based on estrogen receptor status.* Cancer Res, 2010. **70**(11): p. 4759-66.
46. Balaban, S., et al., *Obesity and cancer progression: is there a role of fatty acid metabolism?* Biomed Res Int, 2015. **2015**: p. 274585.
47. Shah, T., et al., *Noninvasive imaging identifies new roles for cyclooxygenase-2 in choline and lipid metabolism of human breast cancer cells.* NMR Biomed, 2012. **25**(5): p. 746-54.
48. Barba, I., M.E. Cabanas, and C. Arus, *The relationship between nuclear magnetic resonance-visible lipids, lipid droplets, and cell proliferation in cultured C6 cells.* Cancer Res, 1999. **59**(8): p. 1861-8.
49. Lupu, J.A.M.a.R., *Fatty acid synthase and the lipogenic phenotype in cancer pathogenesis.* nature reviews, 2007. **7**: p. 14.
50. Alhallak, K., et al., *Optical redox ratio identifies metastatic potential-dependent changes in breast cancer cell metabolism.* Biomed Opt Express, 2016. **7**(11): p. 4364-4374.

Figure Legends

Figure 1. Cellular metabolic changes during formation of acini. Representative ORR **(a, c, e)** and CARS **(b, d, f)** images of acini acquired at days 4, 8 and 12. ORR images provide information about the optical redox ratio distribution inside the acini. Optical redox ratio of the acini is color coded based on the scale bar. CARS images show the lipid volume fraction inside acini **(g)** ORR and lipid content (%) of acini imaged over 12 days. Each data point is an average (+/- SD) of all the cells in 15 randomly chosen acini. The average ORR (diamond) and lipid content (square) increase with respect to time. The scale bar is 10um.

Figure 2. Cross-sectional TPEF (upper row) and CARS (lower row) images of acini of PME (a, d), T47D (b, e) and MDA-MB-231 (c, f) cell lines. (g) Average optical redox ratio (white slash bars) and lipid content (gray solid bars) of three different cell lines are compared, N = 15 acini. (h) lipid content (%) vs ORR shown for each individual acinus consisting of PME (squares), T47D (circles) and MDA-MB-231 (triangles) cell lines. Each point represents an average of all cells in an acinus. Error bars in (g) represent standard error calculated from 15 independent measurements. The scale bar is 10μm.

Figure 3. Morphological and metabolic changes in tumor cell acini following E2 stimulation. (a) Cross sectional images of PME acinus before E2; (b) Cross sectional image of PME acinus after E2. (c) Cross sectional images of T47D acinus before E2; (d) Cross sectional image of T47D acinus after E2. In both images, NADH (green) is excited with two-photon excited fluorescence (TPEF); ECM collagen (blue) is measured with second harmonic generation (SHG); lipid

droplets (red) are imaged with coherent anti-stokes Raman scattering (CARS). The scale bar is 10μm. (e) Summary of glucose and lipid response to E2 stimulation for 10 randomly selected acini composed of T47D breast cancer cells and PME cells. Significant differences in ORR and lipid content (%) are seen between cell lines at baseline and within each line following E2 stimulation. (f) Lipid content (%) vs ORR for PME and T47D cells before and after adding E2. The solid circles and squares are PME and T47D measurements before E2; hollowed circles and squares are measurements after E2. Each single data point represents an average of all the cells in a whole acini structure. The purple arrows indicate the direction of metabolic change induced by adding E2. (g-i) Rose plots showing distribution of collagen fiber orientation angles. Plots were generated from 5 different stacks of spheroids and data binned into 9 angular ranges. (g) collagen fiber angles vs. normal vector of T47D spheroid acini boundaries prior to E2; gold square 1 in (c) shows example ROI. (h) collagen fiber angles vs. normal vector of T47D spheroid cell cluster boundaries in broken acini after E2 treatment; gold square 2 in (d) shows example ROI. (i) collagen fiber angles vs. normal vector of T47D cell extrusion boundaries after E2 treatment; gold square 3 in (d) shows example ROI.

Figure 4. SRS images of normal lipid accumulation from (a) PME cells, (b) T47D cells and (c) T47D cells treated with estradiol. (d) SRS images of deuterated lipid accumulation from PME cells, (e) T47D cells and (f) T47D cells treated with estradiol. Inset of image: zoom-in image of marked area showing the donut-shaped dLD as an indicator for newly synthesized LD. (g) The optical redox ratio (ORR) and normal lipid content (%) for PME cells, T47D cells and T47D cells treated with estradiol. The error bars represent the standard deviation from 25 randomly

picked fields of view. (h) the average intensity ratios of deuterated lipid (dLD) and normal lipid (LD) from PME cells, T47D cells and T47D cells treated with estradiol. (i-k) representative images of deuterated lipids at T=0h, 6h, and 12h. (l) The dLD/LD decay for T47D cells treated with DMSO (blue square) and 17β-estradiol (red circle) over 24 hours. The data points represent deuterated signals measured at time T=0h, 3h, 6h, 9h, and 12h. The solid lines represent exponential decay fitting of the data, dLD/LD=exp(-kt), where k corresponds to the rate at which the lipid signal disappears. The lipid decay rate in cancer cells treated with E2 was k=0.26 ± 0.02 *vs* cells treated with DMSO k=0.18 ± 0.01. At each time point, the deuterated signal and normal lipid signal are manually measured from 50 different lipid droplets in 25 cells on average. The error bars represent the standard deviation from 50 LDs.

Author Manuscript Published OnlineFirst on March 13, 2018; DOI: 10.1158/0008-5472.CAN-17-2618
Author manuscripts have been peer reviewed and accepted for publication but have not yet been edited.

Figure 1

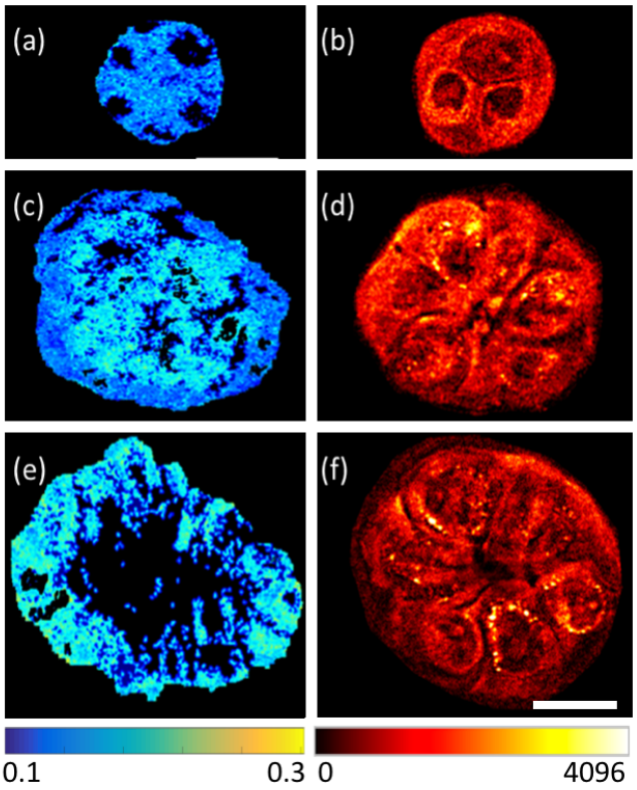

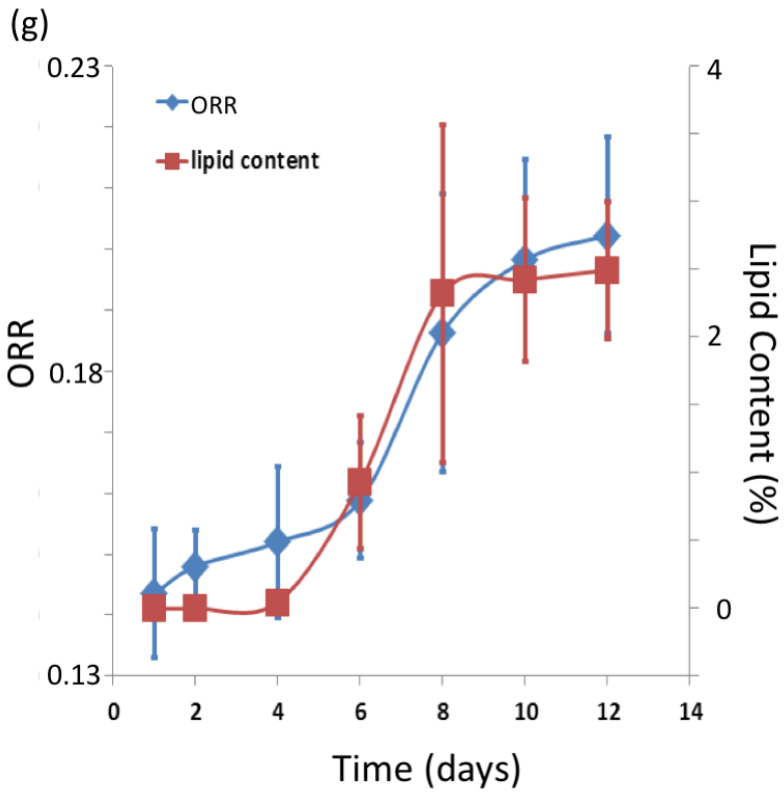

Figure 2

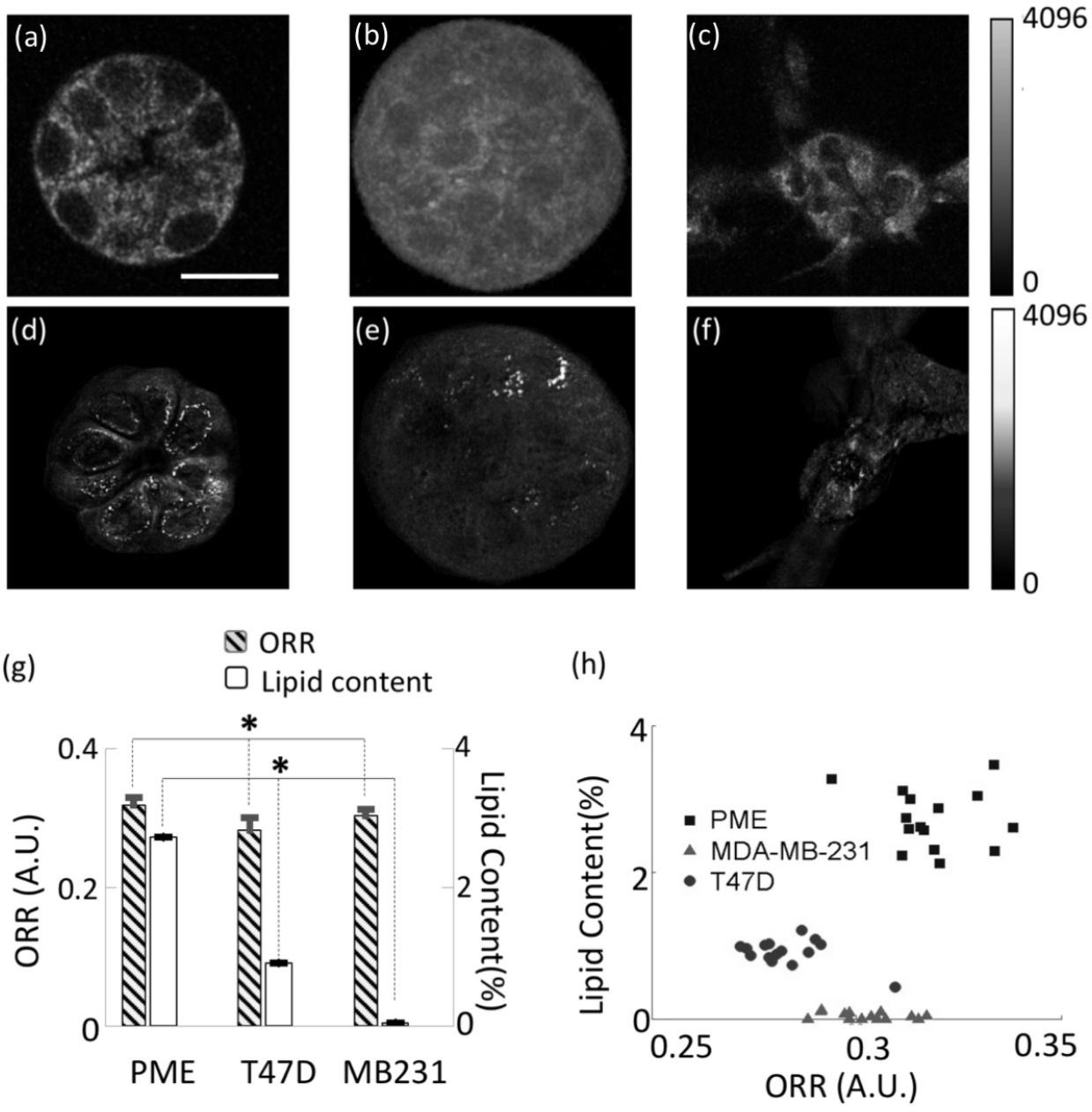

Author Manuscript Published OnlineFirst on March 13, 2018; DOI: 10.1158/0008-5472.CAN-17-2618
Author manuscripts have been peer reviewed and accepted for publication but have not yet been edited.

Figure 3

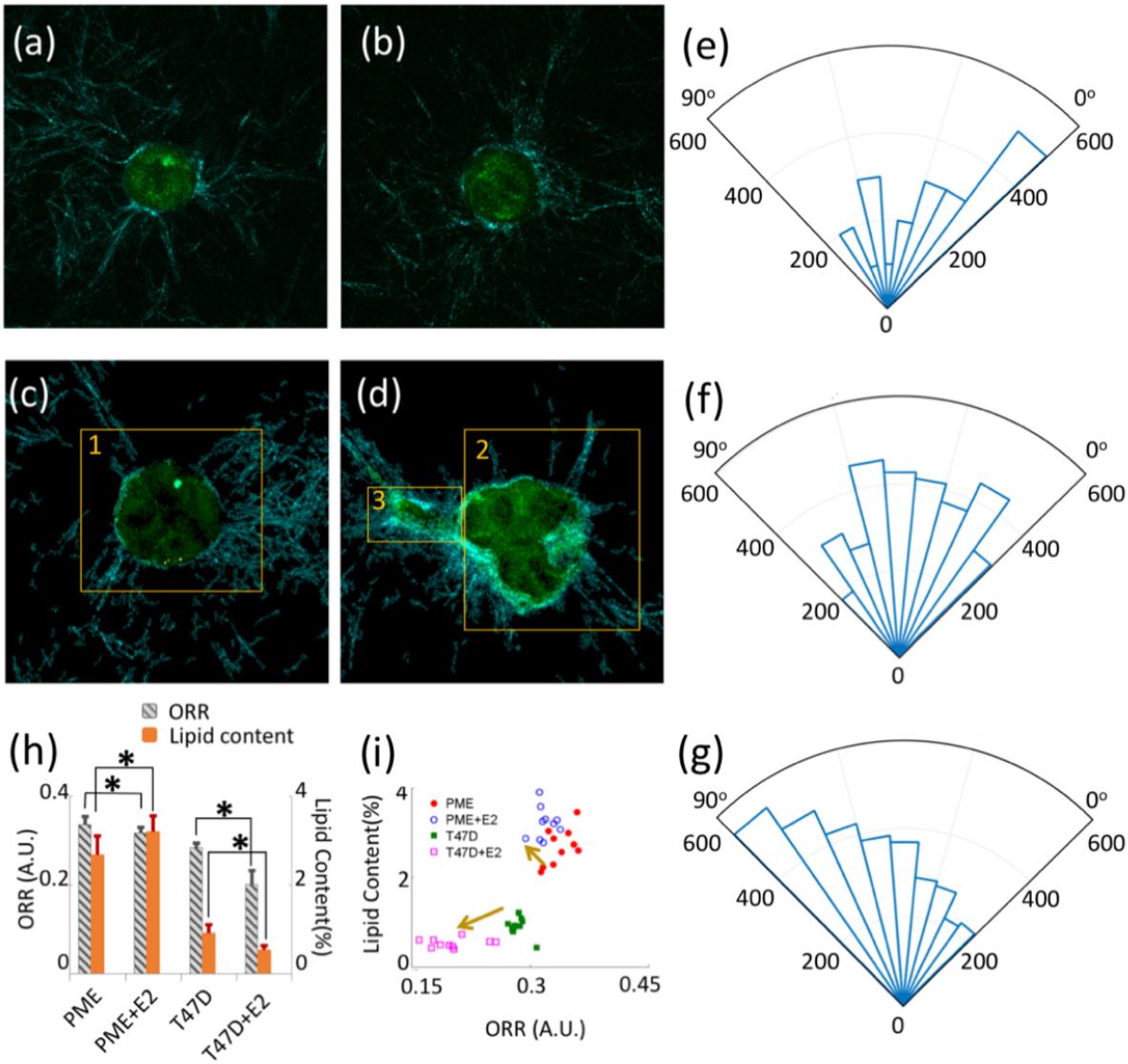

Author Manuscript Published OnlineFirst on March 13, 2018; DOI: 10.1158/0008-5472.CAN-17-2618
Author manuscripts have been peer reviewed and accepted for publication but have not yet been edited.

Figure 4

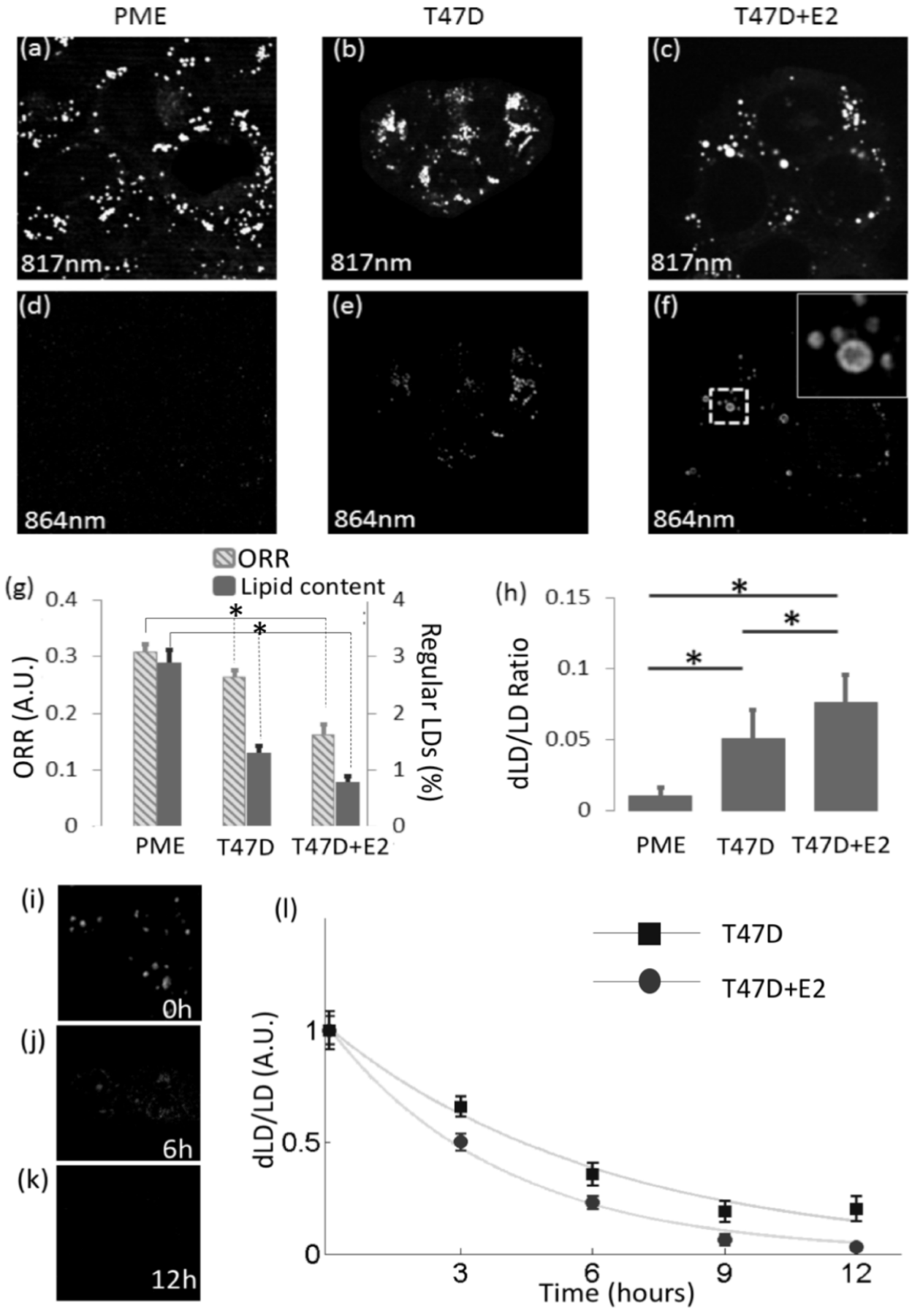

Cancer Research
The Journal of Cancer Research (1916–1930) | The American Journal of Cancer (1931–1940)

AACR American Association for Cancer Research

Visualization of breast cancer metabolism using multimodal non-linear optical microscopy of cellular lipids and redox state

jue hou, Joshua Williams, Elliot Botvinick, et al.

Cancer Res Published OnlineFirst March 13, 2018.